Spin-Twisted Optical Lattices: Tunable Flat Bands and Larkin-Ovchinnikov Superfluids

Xi-Wang Luo* and Chuanwei Zhang†
Department of Physics, The University of Texas at Dallas, Richardson, Texas 75080-3021, USA

(Received 12 August 2020; revised 20 December 2020; accepted 10 February 2021; published 8 March 2021)

Moiré superlattices in twisted bilayer graphene and transition-metal dichalcogenides have emerged as a powerful tool for engineering novel band structures and quantum phases of two-dimensional quantum materials. Here we investigate Moiré physics emerging from twisting two independent hexagonal optical lattices of atomic (pseudo-)spin states (instead of bilayers) that exhibit remarkably different physics from twisted bilayer graphene. We employ a momentum-space tight-binding calculation that includes all range real-space tunnelings and show that all twist angles $\theta \lesssim 6°$ can become magic and support gapped flat bands. Because of the greatly enhanced density of states near the flat bands, the system can be driven to superfluidity by weak attractive interaction. Strikingly, the superfluid phase corresponds to a Larkin-Ovchinnikov state with finite momentum pairing that results from the interplay between flat bands and interspin interactions in the unique single-layer spin-twisted lattice. Our work may pave the way for exploring novel quantum phases and twistronics in cold atomic systems.

DOI: 10.1103/PhysRevLett.126.103201

Introduction.—Twisting two weakly coupled adjacent crystal layers has been employed as a powerful tool for tailoring electronic properties of two-dimensional quantum materials [1–7], e.g., the formation of Moiré superlattices and flat bands. This has been evidenced by the recent groundbreaking discovery of superconductivity and correlated insulator phases in twisted bilayer graphene (TBG) [8,9], which provide a rich platform for exploring strongly correlated many-body phases [10–15], with the underlying physical mechanisms still under investigation [16–26]. In TBG, the interactions, the interlayer and intralayer couplings, are generally fixed with very limited tunability [27–30], and magic flat bands occur only in a narrow range of very small twist angles around $\sim 1.1°$. Going beyond the layer degree of freedom in TBG, two questions naturally arise. Can lattices of other pseudo degrees be twisted to realize novel Moiré lattices and flat bands with great tunability? If so, can new physics emerge in such twisted systems?

Ultracold atoms in optical lattices provide a promising platform for exploring many-body physics in clean environments with versatile tunability [31–47]. While it is challenging to realize twisted bilayer lattices, the atomic internal states offer a pseudospin degree where optical lattice for each spin state can be controlled independently (in particular for alkaline-earth atoms) [48–51], allowing the realization of spin-twisted lattices and related Moiré physics. Such spin-twisted lattices have several remarkable differences from TBG. For instance, two spins reside on one layer spatially (instead of as a bilayer as in TBG) with their coupling provided by additional lasers, resulting in different interspin (compared to interlayer in TBG) hopping and other physical parameters. The interaction is dominated by the interspin s-wave scattering between fermion atoms in relatively twisted spin lattices in contrast to the uniform intralayer interaction without spin twist in TBG. These differences can significantly affect the resulting band structures and many-body quantum states. It is unclear whether extremely flat and gapped bands (i.e., magic-angle behaviors) can exist in a spin-twisted single-layer lattice. If they can, how large of degrees can the magic angle be tuned to? Can new phases emerge from twisted interspin interactions?

In this Letter, we address these important questions by investigating the Moiré physics for cold atoms in two spin-dependent hexagonal lattices twisted by a relative angle with two spin states coupled by additional uniform lasers. Our main results are as follows:

(i) We employ a momentum-space tight-binding method to include all range real-space tunnelings with high accuracy, which is crucial for obtaining the correct flat band structures and low-energy physics.

(ii) Because of the tunability of interspin coupling strength and lattice depth, all twist angles with $\theta \lesssim 6°$ can become magic and support extremely flat and gapped bands. In general, a smaller magic angle requires weaker interspin coupling or a shallower lattice. When θ is too large, no flat bands exist in the whole parameter space due to strong intervalley coupling.

(iii) The system can be driven to the superfluid phase by very weak attractive interactions at magic angles where the flat bands greatly enhance the density of states (DOS). Strikingly, the superfluid phase corresponds to a Larkin-Ovchinnikov (LO) state [52] with nonzero pairing momentum and staggered real-space pairing order at the hexagonal lattice scale, which do not exist in TBG. The superfluid phase results from the interplay between flat bands and the

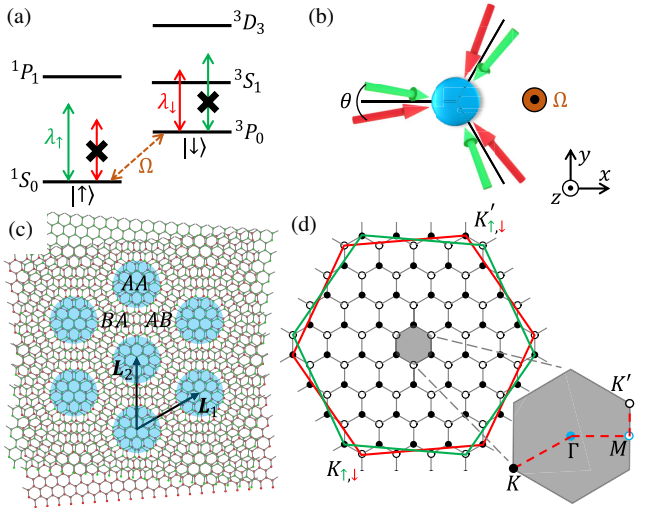

FIG. 1. Scheme for spin-twisted optical lattices. (a) Energy level diagram of alkaline-earth(-like) atoms, showing how state-dependent optical lattices can be realized. (b) Laser configuration to generate spin-twisted hexagonal lattices. (c) Moiré pattern and (d) Brillouin zone of spin-twisted hexagonal lattices with $\theta = 9.43°$ ($m = 3, n = 4$). *AA* spots form a triangle lattice with *AB* or *BA* spots at the triangles' centers. $\boldsymbol{L}_i$ are the primitive lattice vectors. The large hexagons in (d) correspond to the bare BZs for states ↑ (green) and ↓ (red), respectively.

unique interspin interactions of atoms in relatively twisted spin lattices.

Model.—To obtain independent optical lattices that can be twisted, we consider two long-lived $^1S_0$ and $^3P_0$ orbital states (denoted as pseudospin states $|\uparrow\rangle$ and $|\downarrow\rangle$) of alkaline-earth (-like) atoms [48–51], as shown in Fig. 1(a). Atoms in state $|\uparrow(\downarrow)\rangle$ are trapped solely by $\lambda_{\uparrow(\downarrow)}$-wavelength lasers, which are tuned out for atoms in the state $|\downarrow(\uparrow)\rangle$ (e.g., $\lambda_{\uparrow,\downarrow} =$ 627 nm and 689 nm for Sr atoms). A hexagonal lattice $V(\boldsymbol{r}) = -V_0|\sum_{j=1}^{3}\epsilon_j \exp[i\boldsymbol{k}_{L,j}\cdot(\boldsymbol{r}-\boldsymbol{r}_0)]|^2$ is generated by intersecting three lasers at 120° in the x-y plane, with each beam linearly in-plane polarized [37]. Here V_0 is the trap depth, $\boldsymbol{r}_0$ is the hexagonal plaquette center, and $\boldsymbol{k}_{L,j}$ and ϵ_j are the laser wave vector and polarization. Hereafter, we set momentum and energy units as $k_R = 2\pi/\lambda_\downarrow$ and $E_R = \hbar^2 k_R^2/2m$. The two spin-dependent potentials $V_{\uparrow,\downarrow}(\boldsymbol{r})$ are obtained through twisting $V(\boldsymbol{r})$ by $\pm\theta/2$ [see Fig. 1(b)]. The shorter wavelength $\lambda_\uparrow$ lasers have an out-of-plane angle to ensure the same lattice constant for two potentials. The z direction is tightly confined by an additional state-independent potential using the so-called magic-wavelength lasers [35], which reduces the dynamics to two dimensions (2D). The two pseudospin states are coupled by a clock laser [35] propagating along z with Ω the Rabi frequency.

We first consider commensurate twists with $\cos(\theta) = [(n^2+m^2+4mn)/2(n^2+m^2+mn)]$ parameterized by two integers (m, n) [1]. In Fig. 1(c), (d), the real-space pattern and Moiré Brillouin zone (BZ) are shown together with the bare BZs of two spins. For typical lattice depth, long-range tunnelings beyond nearest neighbors (especially for the interspin couplings where the site separations take various values and are nearly continuously distributed for small twists) should be taken into account to obtain the correct magic flat bands [53]. Small deviations in the tunneling coefficients may result in a significant change in the flat band structures due to the narrow bandwidth. Here we adopt the momentum-space Bloch basis $\{\phi_{sl\boldsymbol{k}_s}(\boldsymbol{r})\}$ (with $\boldsymbol{k}_s$ the Bloch momentum, l the band index, and $s = \uparrow, \downarrow$) of $V_s(\boldsymbol{r})$, which spans the same tight-binding Hilbert space as the Wannier basis. When the two spins are decoupled, the lowest two bands of each spin state form two Dirac points for $\boldsymbol{k}_s$ at valley K_s and K'_s in the bare BZs [53].

By projecting onto the basis $\{\phi_{sl\boldsymbol{k}_s}(\boldsymbol{r})\}$, the interspin coupling Hamiltonian reads [53]

$$H_{\uparrow\downarrow}(\boldsymbol{q}) = \sum_{l,l',\mathbf{g}_{\uparrow,\downarrow}} J^{ll'}_{\mathbf{g}_\uparrow\mathbf{g}_\downarrow}(\boldsymbol{q})\alpha^\dagger_{\uparrow l\boldsymbol{q}+\mathbf{g}_\uparrow}\alpha_{\downarrow l'\boldsymbol{q}+\mathbf{g}_\downarrow} + \text{H.c.}, \quad (1)$$

where $\alpha^\dagger_{sl\boldsymbol{k}_s}$ are the creation operators of the Bloch states, $\boldsymbol{q}$ is the superlattice Bloch momentum in the Moiré BZ, and $\mathbf{g}_s$ are the reciprocal lattice vectors of the Moiré superlattice whose summation runs over the bare BZ of state s. The interspin coupling coefficients are $J^{ll'}_{\mathbf{g}_\uparrow\mathbf{g}_\downarrow} = \langle\phi_{\uparrow l\boldsymbol{q}+\mathbf{g}_\uparrow}|\Omega|\phi_{\downarrow l'\boldsymbol{q}+\mathbf{g}_\downarrow}\rangle$, which already incorporate all range real-space tunnelings. Another advantage of this momentum-space approach is that if only the low-energy physics is of interest, then we only need to keep l and $\mathbf{g}_s$ that correspond to the low-energy Bloch states [1–4], leading to a rather rapid convergence of the basis set.

Although spin-twisted optical lattices share some similarities with TBG, several important differences need be noted. (i) The two twisted optical potentials are spin dependent and do not affect each other, while in TBG electrons in one layer can feel the potential of the other layer. (ii) The interspin couplings in the single layer (realized by additional lasers) are different from the interlayer tunnelings in TBG [1,53]. (iii) The optical lattice potential takes a simple cosine form; therefore, the bare bands and interspin couplings can be obtained accurately from the Bloch states. The TBG Hamiltonians are usually based on real-space tight-binding approximations expressed in Slater-Koster parameters [1,54–57]. (iv) Long-range tunnelings are more significant due to the shallow lattices considered here, which not only improve the atomic lifetime but also increase the bare Dirac velocity. (v) Interactions are dominated by the s-wave scattering between fermion atoms in relatively twisted lattices, while electronic interactions in TBG, including both Coulomb repulsive and phonon-mediated attractive interactions, mainly involve electrons in the same layer with no relative twist [16–21]. (vi) Finally, the cold-atom parameters (e.g., interspin tunnelings, lattice depth, lattice constant,

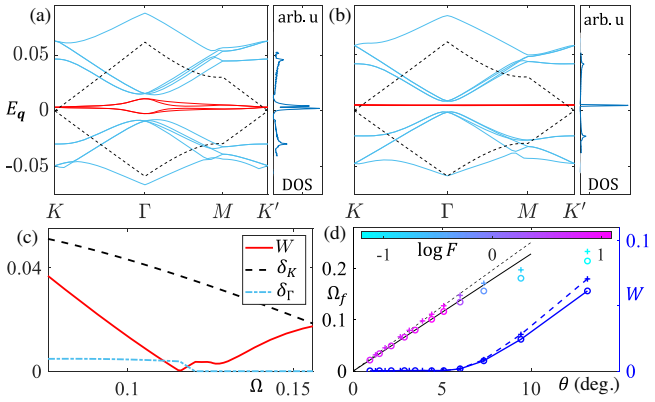

FIG. 2. Magic flat bands. (a),(b) Moiré bands along high-symmetry lines [the red dashed lines in Fig. 1(d)] and DOS for $\Omega = 0.1$ and $\Omega = 0.116$, respectively. We set the bare Dirac cone energy as zero. The black dashed lines are bare Dirac bands folded back to Moiré BZ. (c) Flat band width W and gaps $\delta_{K,\Gamma}$ with other higher bands at K and Γ points. In (a)–(c), $\theta = 5.086°$ and $V_0 = 6$. (d) Critical coupling Ω_f as a function of θ with $V_0 = 6$ (circles) and $V_0 = 4$ (plus signs). Color bars show the flatness at $\Omega = \Omega_f$ with the flat band width shown by the thick blue markers and lines. The thin solid (dashed) line corresponds to $c = 1.932$ at $V_0 = 6$ ($c = 1.827$ at $V_0 = 4$).

interactions, etc.) are highly tunable compared to the one tunable parameter, the twist angle, in TBG.

Flat bands.—We solve the Moiré bands numerically and find that all small twist angles ($\theta \lesssim 6°$) can become magic and support flat bands with the proper choice of interspin coupling strength or lattice depth. In Fig. 2(a), (b), we plot the band structures for different interspin coupling strengths Ω with $V_0 = 6$ and $\theta = 5.086°$ ($m = 6$, $n = 7$). Similar to TBG, the system has four low-energy bands, two of which form a Dirac cone at the Moiré K (K') point where the remaining two bands are split by a tiny gap due to the intervalley (K_s-$K'_{\bar{s}}$) coupling. The Dirac cones shift to a higher energy compared to the bare ones, which is due to the couplings with states away from the valleys that have weak nonlinearity in the dispersion. The interspin coupling reduces the Dirac velocity significantly and enhances the DOS near the Dirac cones, as shown in Fig. 2(a). The peaks in the DOS correspond to the Van Hove singularities near the Moiré M points [21,58]. The bandwidth W of the low-energy bands and Dirac velocity are reduced further as Ω increases and may even vanish (i.e., the twist angle becomes magic) at certain interspin coupling strengths. We are interested in the flat bands associated with magic angles and will focus on the physics around the critical coupling Ω_f where the narrowest bandwidth occurs [as shown in Fig. 2(b)]. For $\Omega \lesssim \Omega_f$, the four low-energy bands are always separated by an energy gap from other bands in the spectrum, the gap is minimized near the Moiré Γ point and would close eventually as we increase Ω above Ω_f. Shown in Fig. 2(c) are the bandwidth W and gaps $\delta_{\Gamma,K}$ (with other higher bands) versus Ω.

In Fig. 2(d), we plot Ω_f and the corresponding bandwidth W and flatness $F \equiv \delta_\Gamma/W$ as functions of the twist angle θ. For small twists, the low-energy bands are mainly determined by the states with $\mathbf{g}_s$ around the Dirac valleys, and have a narrow width and high flatness at $\Omega = \Omega_f$. In addition, the intervalley coupling is weak; thus, two conduction or valence bands (one from each valley) are nearly degenerate along the high-symmetric Γ-K (K') lines [21]. We find Ω_f almost linearly increases with θ. Specifically, the magic flat bands occur near $c = \text{const}$, where $c \equiv \Omega/(v_D k_D)$ is a dimensionless parameter with $k_D = 2k_R \sin(\theta/2)$ the K-K' distance in Moiré BZ and v_D the bare Dirac velocity. This is consistent with the continuum model in TBG where c is the single parameter [3,4]. When the twist angles are large $\theta > 6°$, the width and splitting of the four low-energy bands become comparable or larger than the gap with other bands, and no magic flat bands exist for any Ω since the intervalley couplings and the effects of states away from the bare Dirac valleys become significant. For incommensurate twist angles, we can generalize the continuum model and only keep $\mathbf{g}_s$ around one valley, which should be valid for small θ [53]. We thus conclude that all small angles $\theta \lesssim 6°$ can support magic flat bands.

For different lattice depths V_0, the magic behaviors discussed above are similar [see Fig. 2(d)]. Meanwhile, a smaller V_0 leads to a larger v_D and thereby a stronger Ω_f (for fixed θ). Long-range tunnelings are also more significant in a shallower lattice, which would effectively enhance the interspin couplings, leading to a slightly smaller c where the flat bands occur. The flatness may also be improved by decreasing V_0 properly, since a larger v_D leads to a larger gap δ_Γ [3,4] and long-range tunnelings in real space can reduce intervalley couplings that have large momentum separations. However, in the very shallow region where the dispersion linearity around the bare Dirac cone becomes poor, the flatness starts to decrease with V_0.

Superfluid orders.—The narrowly dispersing flat bands suppress the kinetic energy, and atom-atom interactions can lead to strongly correlated many-body ground states. Unlike TBG [16–21], here the interaction of fermion atoms is dominated by s-wave scattering between atoms in relatively twisted lattices, with strength tunable through Feshbach resonance [46,47],

$$H_{\text{int}} = U_0 \int d^2\boldsymbol{r} \hat{\Psi}^\dagger_\uparrow(\boldsymbol{r})\hat{\Psi}^\dagger_\downarrow(\boldsymbol{r})\hat{\Psi}_\downarrow(\boldsymbol{r})\hat{\Psi}_\uparrow(\boldsymbol{r}). \tag{2}$$

We are interested in the superfluid order driven by attractive interactions. We adopt the mean-field approach [16–18] with local pairing amplitude $\Delta(\boldsymbol{r}) = U_0\langle\hat{\Psi}_\downarrow(\boldsymbol{r})\hat{\Psi}_\uparrow(\boldsymbol{r})\rangle$ and assume that it has Moiré periodicity [18], which can therefore be expanded in the form $\Delta(\boldsymbol{r}) = \sum_{\mathbf{g}} \Delta_{\mathbf{g}} e^{i\mathbf{g}\cdot\boldsymbol{r}}$ with $\mathbf{g}$ the Moiré reciprocal lattice vectors. We use the Bogoliubov-de Gennes Hamiltonian to obtain $\Delta(\mathbf{r})$

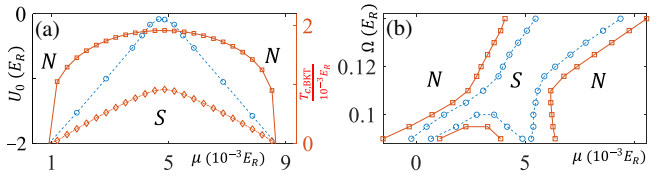

FIG. 3. Phase diagrams for attractive interactions. (a) Phase diagrams in the U_0-μ plane at zero temperature (blue dots). The critical temperatures T_c (red squares) and T_{BKT} (red diamonds) as functions of μ at $U_0 = -2$, with $\Omega = \Omega_f$. (b) Zero-temperature phase diagrams in the Ω-μ plane for $U_0 = -0.5$ (blue dots) and $U_0 = -1$ (red squares). N and S represent the normal and superfluid phases, respectively. Common parameters: $\theta = 5.086°$, $V_0 = 6$.

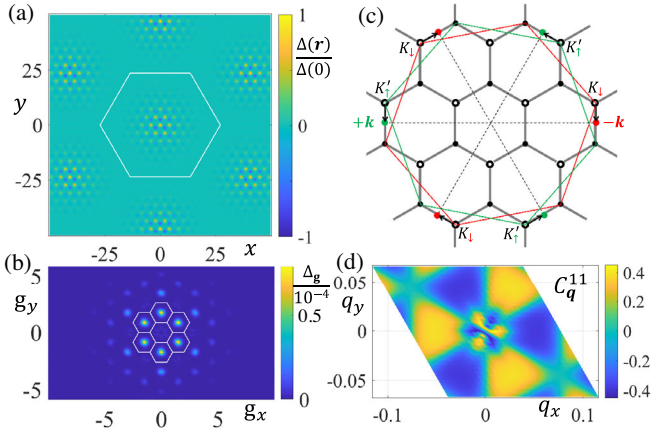

FIG. 4. Superfluid orders. (a),(b) The superfluid pairing amplitudes in real [$\Delta(\boldsymbol{r})$] and momentum space ($\Delta_{\mathbf{g}}$), respectively. The white hexagons correspond to the Moiré unit cell in (a) and the untwisted bare BZs in (b). (c) Schematic illustration of the pairing (indicated by dashed lines) in the BZs. (d) The correlation $C_{\boldsymbol{q}}^{11}$. Common parameters: $\theta = 5.086°$, $V_0 = 6$, $\Omega = \Omega_f$, and $U_0 = -0.5$.

self-consistently [53] and retain only the four flat bands that have a much larger DOS than nearby bands. We have verified that the physics is hardly affected by numerically including more nearby bands [53].

The phase diagrams for $\theta = 5.086°$, $V_0 = 6$, and $\Omega = \Omega_f$ are shown in Fig. 3(a). Because of the greatly enhanced DOS near the magic flat bands at Ω_f, the system could be driven to superfluidity by very weak attractive interaction $|U_0| \lesssim 0.08$ (at zero temperature) when the chemical potential matches the flat band energy. As μ is tuned away from flat bands, the required interaction strength for the superfluid phase increases (almost linearly). For a moderate interaction strength, the mean-field critical temperature T_c could be relatively high (it reaches its largest value at $\mu \simeq 0.005$) and shows a similar behavior as that predicted in the TBG system [18].

Note that, at finite temperature, the relevant physics in 2D is the Berezinskii-Kosterlitz-Thouless (BKT) transition [59–62] because no long-range superfluid order exists due to phase fluctuations, and the mean-field T_c is often overestimated. The BKT critical temperature T_{BKT} could be obtained from the mean-field superfluid weight [53,63,64], which is numerically calculated with the results shown in Fig. 3(a) (roughly, $T_{\mathrm{BKT}} \simeq 0.4T_c$).

In Fig. 3(b), we plot the phase diagrams in the Ω-μ plane. Away from Ω_f, the bandwidth will be broadened, and the superfluid area becomes wider. However, it requires a lower critical temperature or stronger interaction due to the reduced DOS. At the $\Omega < \Omega_f$ side, the flat band DOS peak splits into two peaks (corresponding to the Van Hove singularities near the Moiré M points), and therefore the superfluid phase also splits into two regions where μ matches the DOS peaks. At the $\Omega > \Omega_f$ side, the DOS peak is simply broadened. As the $|U_0|$ decreases, the superfluid phase shrinks to the area around $\Omega \simeq \Omega_f$ and $\mu \simeq 0.005$.

Strikingly, we find that the superfluid phase corresponds to an LO state [52], which is very different from that in TBG. The Cooper pairs have a nonzero center-of-mass momentum with $\Delta_{\mathbf{g}}$ mainly distributed around the first reciprocal lattice vector shell of the untwisted hexagonal lattice and nearly vanishing around zero momentum, leading to the staggered real-space pairing orders at the hexagonal lattice scale [Fig. 4(a), (b)]. The attractive s-wave interaction pairs atoms from opposite valleys, and the superfluid order is peaked in the AA regions, where the local DOS for the flat bands is strongly concentrated [53] and the wave function overlap between two spin states is significant. Therefore, the intrasublattice pairing is dominant. Because atoms at the same sublattices and opposite valleys share opposite angular momenta under the threefold rotation, the pairing order has the same phase factor for the same sublattice.

Moreover, the pairing is between Moiré states at $\pm\boldsymbol{q}$, which are mainly determined by the bare Bloch states $\phi_{sl\pm\boldsymbol{k}}$ at $\pm\boldsymbol{k}$ nearest to the valleys (thereby contributing most to the flat bands). In Fig. 4(c), the pairing between $\uparrow$ states (green dots at $+\boldsymbol{k}$) around valley $K'_\uparrow$ and $\downarrow$ states (red dots at $-\boldsymbol{k}$) around valley $K_\downarrow$ is illustrated schematically. Due to the relative twist, $\pm\boldsymbol{k}$ are at the same side of $K'_\uparrow$ and $K_\downarrow$, respectively [see the black arrows in Fig. 4(c)]. Therefore, we have $\phi_{\uparrow lk} \propto [1, e^{i\gamma_{\uparrow k}}]^T$ and $\phi_{\downarrow l(-k)} \propto [1, e^{i\gamma_{\downarrow(-k)}}]^T$ on the A and B sublattice basis, with $\gamma_{\uparrow k} \simeq -\gamma_{\downarrow(-k)} + \pi$. The relative phases γ_{sk} are related to the chirality of the valleys (i.e., the Berry phase on loops surrounding the valley), which are responsible for the staggered pairing order $\Delta(\boldsymbol{r}) \propto \langle \phi_{\uparrow lk}\phi_{\downarrow l(-k)}\rangle \propto [1, -1]^T$ [53]. Such the LO order is unique for a spin-twisted system with pairing between atoms from relatively twisted lattices. In TBG, the pairing between spin-up and spin-down electrons in the same layer (with no relative twist) leads to ordinary BCS order [17,18].

The correlation $C_{\boldsymbol{q}}^{j'j} = \langle \beta_{j'-\boldsymbol{q}}\beta_{j\boldsymbol{q}}\rangle$ shows f-wave structure ($\beta_{j\boldsymbol{q}}$ is the annihilation operator for the jth flat band), their

combined effects lead to the nearly uniform superfluid gap [53] and the pairing is s wave. The valence bands from different valleys become degenerate along the high symmetric Γ-K lines with avoided crossing (a tiny gap) due to intervalley couplings; therefore, $C_{\boldsymbol{q}}^{11}$ changes from characterizing K_s-$K'_{\bar{s}}$ to $K'_{\bar{s}}$-K_s correlations across the Γ-K lines where its sign flips [see Fig. 4(d)].

Discussion and conclusion.—Due to the high tunability of the cold-atom system, the "magic-angle" physics in the spin-twisted optical lattice is very robust, supporting magic flat bands and novel LO superfluid order in a wide range of parameter space (θ, V_0, Ω, U_0, etc.). For $\theta \simeq 5°$ and $V_0 = 6$, the gap between flat bands and other bands is $\sim 10^{-2} E_R$ (about tens of Hz for Sr atoms) and can be improved further using shallower lattices (larger v_D) or larger twists. The flat bands and enhanced DOS can be observed within the atomic gas lifetime (a few seconds for the shallow lattice considered here) using spectroscopic measurements (e.g., radio-frequency spectroscopy) [65–68]. The critical superfluid temperature $T_{c,\mathrm{BKT}}$ is in the nanokelvin region ($\sim 10^{-3} E_R$), which might be possible with the recently developing cold-atom cooling techniques [33,69–71]. Thanks to the large twist angle $\theta \lesssim 6°$, the Moiré unit cell may contain fewer than 100 hexagons; therefore, the magic phenomena can be observed using a small system with tens of hexagons along each direction. The magic-angle physics is similar for different stackings or twist axes [53].

In summary, we study the Moiré flat band physics and the associated superfluid order in spin-twisted optical lattices for ultracold atoms, which showcase magic-angle behaviors for a continuum of twists up to 6° and a novel LO superfluid phase remarkably different from that in TBG. In the future, it would be interesting to study spin-twisted lattices of other types (square, triangle, etc.) or with different lattice depths and gapped bands (similar to transition metal dichalcogenide-based Moiré systems [72,73]). Moreover, one could study possibly interesting many-body states under repulsive interaction and may even consider the nuclear spin states of alkaline-earth atoms with nuclear-spin-exchange and interspin interactions. In all, our work provides a highly tunable playground for exploring quantum many-body physics and twistronics with novel twisted pseudo degrees of freedom.

We thank J. H. Pixley for helpful discussions. This work is supported by AFOSR (FA9550-16-1-0387, FA9550-20-1-0220), NSF (PHY-1806227), and ARO (W911NF-17-1-0128).

*Corresponding author.
xiwang.luo@utdallas.edu
†Corresponding author.
chuanwei.zhang@utdallas.edu

[1] J. M. B. Lopes dos Santos, N. M. R. Peres, and A. H. Castro Neto, Graphene Bilayer with a Twist: Electronic Structure, Phys. Rev. Lett. **99**, 256802 (2007).
[2] S. Shallcross, S. Sharma, E. Kandelaki, and O. A. Pankratov, Electronic structure of turbostratic graphene, Phys. Rev. B **81**, 165105 (2010).
[3] R. Bistritzer and A. H. MacDonald, Moiré bands in twisted double-layer graphene, Proc. Natl. Acad. Sci. U.S.A. **108**, 12233 (2011).
[4] J. M. B. Lopes dos Santos, N. M. R. Peres, and A. H. Castro Neto, Continuum model of the twisted graphene bilayer, Phys. Rev. B **86**, 155449 (2012).
[5] G. T. de Laissardière, D. Mayou, and L. Magaud, Localization of Dirac electrons in rotated graphene bilayers, Nano Lett. **10**, 804 (2010).
[6] Y. Cao, J. Y. Luo, V. Fatemi, S. Fang, J. D. Sanchez-Yamagishi, K. Watanabe, T. Taniguchi, E. Kaxiras, and P. Jarillo-Herrero, Superlattice-Induced Insulating States and Valley-Protected Orbits in Twisted Bilayer Graphene, Phys. Rev. Lett. **117**, 116804 (2016).
[7] F. Hu, S. R. Das, Y. Luan, T.-F. Chung, Y. P. Chen, and Z. Fei, Real-Space Imaging of the Tailored Plasmons in Twisted Bilayer Graphene, Phys. Rev. Lett. **119**, 247402 (2017).
[8] Y. Cao, V. Fatemi, S. Fang, K. Watanabe, T. Taniguchi, E. Kaxiras, and P. Jarillo-Herrero, Unconventional superconductivity in magic-angle graphene superlattices, Nature (London) **556**, 80 (2018).
[9] Y. Cao, V. Fatemi, A. Demir, S. Fang, S. L. Tomarken, J. Y. Luo, J. D. Sanchez-Yamagishi, K. Watanabe, T. Taniguchi, E. Kaxiras, R. C. Ashoori, and P. Jarillo-Herrero, Correlated insulator behaviour at half-filling in magic-angle graphene superlattices, Nature (London) **556**, 80 (2018).
[10] A. Kerelsky, L. J. McGilly, D. M. Kennes, L. Xian, M. Yankowitz, S. Chen, K. Watanabe, T. Taniguchi, J. Hone, C. Dean, A. Rubio, and A. N. Pasupathy, Maximized electron interactions at the magic angle in twisted bilayer graphene, Nature (London) **572**, 95 (2019).
[11] A. L. Sharpe, E. J. Fox, A. W. Barnard, J. Finney, K. Watanabe, T. Taniguchi, M. A. Kastner, and D. Goldhaber-Gordon, Emergent ferromagnetism near three-quarters filling in twisted bilayer graphene, Science **365**, 605 (2019).
[12] E. Codecido, Q. Wang, R. Koester, S. Che, H. Tian, R. Lv, S. Tran, K. Watanabe, T. Taniguchi, F. Zhang, M. Bockrath, and C. N. Lau, Correlated insulating and superconducting states in twisted bilayer graphene below the magic angle, Sci. Adv. **5**, eaaw9770 (2019).
[13] Y. Choi, J. Kemmer, Y. Peng, A. Thomson, H. Arora, R. Polski, Y. Zhang, H. Ren, J. Alicea, G. Refael, F. von Oppen, K. Watanabe, T. Taniguchi, and S. Nadj-Perge, Electronic correlations in twisted bilayer graphene near the magic angle, Nat. Phys. **15**, 1174 (2019).
[14] G. Chen, L. Jiang, S. Wu, B. Lyu, H. Li, B. L. Chittari, K. Watanabe, T. Taniguchi, Z. Shi, J. Jung, Y. Zhang, and F. Wang, Evidence of a gate-tunable Mott insulator in a trilayer graphene moiré superlattice, Nat. Phys. **15**, 237 (2019).
[15] G. W. Burg, J. Zhu, T. Taniguchi, K. Watanabe, A. H. MacDonald, and E. Tutuc, Correlated Insulating States in Twisted Double Bilayer Graphene, Phys. Rev. Lett. **123**, 197702 (2019).

[16] T. J. Peltonen, R. Ojajärvi, and T. T. Heikkilä, Mean-field theory for superconductivity in twisted bilayer graphene, Phys. Rev. B **98**, 220504(R) (2018).

[17] B. Lian, Z. Wang, and B. A. Bernevig, Twisted Bilayer Graphene: A Phonon-Driven Superconductor, Phys. Rev. Lett. **122**, 257002 (2019).

[18] F. Wu, A. H. MacDonald, and I. Martin, Theory of Phonon-Mediated Superconductivity in Twisted Bilayer Graphene, Phys. Rev. Lett. **121**, 257001 (2018).

[19] H. Isobe, N. F. Q. Yuan, and L. Fu, Unconventional Superconductivity and Density Waves in Twisted Bilayer Graphene, Phys. Rev. X **8**, 041041 (2018).

[20] C.-C. Liu, L.-D. Zhang, W.-Q. Chen, and F. Yang, Chiral Spin Density Wave and $d+id$ Superconductivity in the Magic-Angle-Twisted Bilayer Graphene, Phys. Rev. Lett. **121**, 217001 (2018).

[21] J. González and T. Stauber, Kohn-Luttinger Superconductivity in Twisted Bilayer Graphene, Phys. Rev. Lett. **122**, 026801 (2019).

[22] C. Xu and L. Balents, Topological Superconductivity in Twisted Multilayer Graphene, Phys. Rev. Lett. **121**, 087001 (2018).

[23] X. Hu, T. Hyart, D. I. Pikulin, and E. Rossi, Geometric and Conventional Contribution to the Superfluid Weight in Twisted Bilayer Graphene, Phys. Rev. Lett. **123**, 237002 (2019).

[24] D. M. Kennes, J. Lischner, and C. Karrasch, Strong correlations and $d+id$ superconductivity in twisted bilayer graphene, Phys. Rev. B **98**, 241407(R) (2018).

[25] J. F. Dodaro, S. A. Kivelson, Y. Schattner, X. Q. Sun, and C. Wang, Phases of a phenomenological model of twisted bilayer graphene, Phys. Rev. B **98**, 075154 (2018).

[26] H. C. Po, L. Zou, A. Vishwanath, and T. Senthil, Origin of Mott Insulating Behavior and Superconductivity in Twisted Bilayer Graphene, Phys. Rev. X **8**, 031089 (2018).

[27] K. Kim, A. DaSilva, S. Huang, B. Fallahazad, S. Larentis, T. Taniguchi, K. Watanabe, B. J. LeRoy, A. H. MacDonald, and E. Tutuc, Tunable moiré bands and strong correlations in small-twist-angle bilayer graphene, Proc. Natl. Acad. Sci. U.S.A. **114**, 3364 (2017).

[28] S. Carr, S. Fang, P. Jarillo-Herrero, and E. Kaxiras, Pressure dependence of the magic twist angle in graphene superlattices, Phys. Rev. B **98**, 085144 (2018).

[29] M. Yankowitz, J. Jung, E. Laksono, N. Leconte, B. L. Chittari, K. Watanabe, T. Taniguchi, S. Adam, D. Graf, and C. R. Dean, Dynamic band-structure tuning of graphene moire superlattices with pressure, Nature (London) **557**, 404 (2018).

[30] M. Yankowitz, S. Chen, H. Polshyn, Y. Zhang, K. Watanabe, T. Taniguchi, D. Graf, A. F. Young, and C. R. Dean, Tuning superconductivity in twisted bilayer graphene, Science **363**, 1059 (2019).

[31] D. Jaksch, C. Bruder, J. I. Cirac, C. W. Gardiner, and P. Zoller, Cold Bosonic Atoms in Optical Lattices, Phys. Rev. Lett. **81**, 3108 (1998).

[32] M. Lewenstein, A. Sanpera, V. Ahufinger, B. Damski, A. Sen, and U. Sen, Ultracold atomic gases in optical lattices: Mimicking condensed matter physics and beyond, Adv. Phys. **56**, 243 (2007).

[33] T. Esslinger, Fermi-Hubbard physics with atoms in an optical lattice, Annu. Rev. Condens. Matter Phys. **1**, 129 (2010).

[34] I. Bloch, J. Dalibard, and S. Nascimbène, Quantum simulations with ultracold quantum gases, Nat. Phys. **8**, 267 (2012).

[35] A. D. Ludlow, M. M. Boyd, J. Ye, E. Peik, and P. O. Schmidt, Optical atomic clocks, Rev. Mod. Phys. **87**, 637 (2015).

[36] L. Tarruell, D. Greif, T. Uehlinger, G. Jotzu, and T. Esslinger, Creating, moving and merging Dirac points with a Fermi gas in a tunable honeycomb lattice, Nature (London) **483**, 302 (2012).

[37] T. Li, L. Duca, M. Reitter, F. Grusdt, E. Demler, M. Endres, M. Schleier-Smith, I. Bloch, and U. Schneider, Bloch state tomography using Wilson lines, Science **352**, 1094 (2016).

[38] T. Akatsuka, M. Takamoto, and H. Katori, Optical lattice clocks with non-interacting bosons and fermions, Nat. Phys. **4**, 954 (2008).

[39] S. L. Campbell, R. B. Hutson, G. E. Marti, A. Goban, N. Darkwah Oppong, R. L. McNally, L. Sonderhouse, J. M. Robinson, W. Zhang, B. J. Bloom, and J. Ye, A Fermi-degenerate three-dimensional optical lattice clock, Science **358**, 90 (2017).

[40] L. F. Livi, G. Cappellini, M. Diem, L. Franchi, C. Clivati, M. Frittelli, F. Levi, D. Calonico, J. Catani, M. Inguscio, and L. Fallani, Synthetic Dimensions and Spin-Orbit Coupling with an Optical Clock Transition, Phys. Rev. Lett. **117**, 220401 (2016).

[41] S. Kolkowitz, S. L. Bromley, T. Bothwell, M. L. Wall, G. E. Marti, A. P. Koller, X. Zhang, A. M. Rey, and J. Ye, Spin-orbit-coupled fermions in an optical lattice clock, Nature (London) **542**, 66 (2017).

[42] T. Graß, R. W. Chhajlany, L. Tarruell, V. Pellegrini, and M. Lewenstein, Proximity effects in cold atom artificial graphene, 2D Mater. **4**, 015039 (2016).

[43] Y. Fu, E. J. König, J. H. Wilson, Y.-Z. Chou, and J. H. Pixley, Magic-angle semimetals, npj Quantum Mater. **5**, 71 (2020).

[44] Y.-Z. Chou, Y. Fu, J. H. Wilson, E. J. König, and J. H. Pixley, Magic-angle semimetals with chiral symmetry, Phys. Rev. B **101**, 235121 (2020).

[45] T. Salamon, A. Celi, R. W. Chhajlany, I. Frérot, M. Lewenstein, L. Tarruell, and D. Rakshit, Simulating Twistronics without a Twist, Phys. Rev. Lett. **125**, 030504 (2020).

[46] C. Chin, R. Grimm, P. Julienne, and E. Tiesinga, Feshbach resonances in ultracold gases, Rev. Mod. Phys. **82**, 1225 (2010).

[47] R. Zhang, Y. Cheng, P. Zhang, and H. Zhai, Controlling the interaction of ultracold alkaline-earth atoms, Nat. Rev. Phys. **2**, 213 (2020).

[48] S. G. Porsev, A. D. Ludlow, M. M. Boyd, and J. Ye, Determination of Sr properties for a high-accuracy optical clock, Phys. Rev. A **78**, 032508 (2008).

[49] A. J. Daley, M. M. Boyd, J. Ye, and P. Zoller, Quantum Computing with Alkaline-Earth-Metal Atoms, Phys. Rev. Lett. **101**, 170504 (2008).

[50] L. Riegger, N. Darkwah Oppong, M. Höfer, D. R. Fernandes, I. Bloch, and S. Fölling, Localized Magnetic Moments with Tunable Spin Exchange in a Gas of Ultracold Fermions, Phys. Rev. Lett. **120**, 143601 (2018).

[51] A. González-Tudela and J. I. Cirac, Cold atoms in twisted-bilayer optical potentials, Phys. Rev. A **100**, 053604 (2019).

[52] A. I. Larkin and Y. N. Ovchinnikov, Nonuniform state of superconductors, Zh. Eksp. Teor. Fiz. **47**, 1136 (1964) [Sov. Phys. JETP **20**, 762 (1965)].
[53] See Supplemental Material at http://link.aps.org/supplemental/10.1103/PhysRevLett.126.103201 for more details about Moiré tight-binding Hamiltonian, superfluid orders, the effects of different stackings or twist axes, and the differences between our system and the TBG system.
[54] P. Moon and M. Koshino, Energy spectrum and quantum Hall effect in twisted bilayer graphene, Phys. Rev. B **85**, 195458 (2012).
[55] T. Nakanishi and T. Ando, Conductance of crossed carbon nanotubes, J. Phys. Soc. Jpn. **70**, 1647 (2001).
[56] J. C. Slater and G. F. Koster, Simplified LCAO method for the periodic potential problem, Phys. Rev. **94**, 1498 (1954).
[57] S. Fang and E. Kaxiras, Electronic structure theory of weakly interacting bilayers, Phys. Rev. B **93**, 235153 (2016).
[58] N. F. Q. Yuan, H. Isobe, and L. Fu, Magic of high-order van Hove singularity, Nat. Commun. **10**, 5769 (2019).
[59] V. L. Berezinskii, Destruction of long-range order in one-dimensional and two-dimensional systems having a continuous symmetry group I. Classical systems, Sov. Phys. JETP **32**, 493 (1971).
[60] J. M. Kosterlitz and D. Thouless, Long range order and metastability in two dimensional solids and superfluids. (Application of dislocation theory), J. Phys. C **5**, L124 (1972).
[61] M. Gong, G. Chen, S. Jia, and C. Zhang, Searching for Majorana Fermions in 2D Spin-Orbit Coupled Fermi Superfluids at Finite Temperature, Phys. Rev. Lett. **109**, 105302 (2012).
[62] Y. Xu and C. Zhang, Berezinskii-Kosterlitz-Thouless Phase Transition in 2D Spin-Orbit-Coupled Fulde-Ferrell Superfluids, Phys. Rev. Lett. **114**, 110401 (2015).
[63] X.-J. Liu, K. T. Law, and T. K. Ng, Realization of 2D Spin-Orbit Interaction and Exotic Topological Orders in Cold Atoms, Phys. Rev. Lett. **112**, 086401 (2014).
[64] A. Julku, L. Liang, and P. Törmä, Superfluid weight and Berezinskii-Kosterlitz-Thouless temperature of spin-imbalanced and spin-orbit-coupled Fulde-Ferrell phases in lattice systems, New J. Phys. **20**, 085004 (2018).
[65] C. Chin, M. Bartenstein, A. Altmeyer, S. Riedl, S. Jochim, J. H. Denschlag, and R. Grimm, Observation of the pairing gap in a strongly interacting fermi fas, Science **305**, 1128 (2004).
[66] J. T. Stewart, J. P. Gaebler, and D. S. Jin, Using photoemission spectroscopy to probe a strongly interacting Fermi gas, Nature (London) **454**, 744 (2008).
[67] C. H. Schunck, Y. Shin, A. Schirotzek, and W. Ketterle, Determination of the fermion pair size in a resonantly interacting superfluid, Nature (London) **454**, 739 (2008).
[68] J. Zhang, H. Hu, X.-J. Liu, and H. Pu, Fermi gases with synthetic spin–orbit coupling, Annu. Rev. Cold At. Mol. **2**, 81 (2014).
[69] D. Greif, T. Uehlinger, G. Jotzu, L. Tarruell, and T. Esslinger, Short-range quantum magnetism of ultracold fermions in an optical lattice, Science **340**, 1307 (2013).
[70] A. Mazurenko, C. S. Chiu, G. Ji, M. F. Parsons, M. Kanász-Nagy, R. Schmidt, F. Grusdt, E. Demler, D. Greif, and M. Greiner, A cold-atom Fermi-Hubbard antiferromagnet, Nature (London) **545**, 462 (2017).
[71] B. Yang, H. Sun, C.-J. Huang, H.-Y. Wang, Y. Deng, H.-N. Dai, Z.-S. Yuan, and J.-W. Pan, Cooling and entangling ultracold atoms in optical lattices, Science **369**, 550 (2020).
[72] F. Wu, T. Lovorn, E. Tutuc, and A. H. MacDonald, Hubbard Model Physics in Transition Metal Dichalcogenide Moiré Bands, Phys. Rev. Lett. **121**, 026402 (2018).
[73] Y. Tang, L. Li, T. Li, Y. Xu, S. Liu, K. Barmak, K. Watanabe, T. Taniguchi, A. H. MacDonald, J. Shan, and K. F. Mak, Simulation of Hubbard model physics in WSe2/WS2 moiré superlattices, Nature (London) **579**, 353 (2020).